JOURNAL OF SPACECRAFT AND ROCKETS
Vol. 48, No. 1, January–February 2011

# Numerical Analysis on Oscillation Characteristics in a Tailpipe Nozzle Solid Rocket Motor

Qiao Zhang,* Jun-wei Li,† Wei-chen Wang,‡ and Ning-fei Wang§
*Beijing Institute of Technology, 100081 Beijing, People's Republic of China*

DOI: 10.2514/1.48867

**Based on vortex–acoustic coupling theory, large-eddy simulation with wall-adapting local eddy-viscosity model and finite element method are carried out to study the internal flowfield and acoustic field, respectively, in a tailpipe nozzle solid rocket motor with transition-section grain configuration. The numerical method by means of a mesh sensitivity analysis is proposed for validation. The instantaneous flowfield characteristics in the combustion chamber and tailpipe are analyzed. The excited low frequencies are close to that observed in experiment. The phenomenon in which acoustic signals, superimposed on the vortex-shedding motions, couple with an internal flowfield is proven to be one of the main reasons contributing to oscillation in the motor. According to fast Fourier transform, low frequencies predominate in the combustion chamber; however, high frequencies predominate in the tailpipe. Dozens of cases with different geometrical configurations are presented to investigate parameters that have impact on the low-frequency oscillation characteristics. The results indicate that the oscillation characteristics are mainly influenced by upstream mean velocity, transition-section angle, distance between vortex source and impingement points, tailpipe radius, and convergence angle of the nozzle.**

## Nomenclature

| | | |
|---|---|---|
| $a$ | = | speed of sound, m/s |
| $e$ | = | total specific energy |
| $f$ | = | frequency, Hz |
| $H$ | = | enthalpy, J |
| $M$ | = | molecular weight, g/mol |
| $\dot{m}$ | = | mass flux, $kg/m^2 \cdot s$ |
| $Pr$ | = | Prandtl number |
| $p$ | = | pressure |
| $R$ | = | gas constant |
| $T$ | = | temperature, K |
| $t$ | = | time, s |
| $u$ | = | velocity, m/s |
| $y$ | = | distance from computational cell to wall |
| $\gamma$ | = | ratio of specific heats |
| $\mu$ | = | dynamic viscosity, $kg/m \cdot s$ |
| $\rho$ | = | density, $kg/m^3$ |
| $\sim$ | = | Favre-averaged quantity |
| $-$ | = | Reynolds-averaged quantity |

*Subscripts*

| | | |
|---|---|---|
| $c$ | = | centerline |
| $i, j, k$ | = | Cartesian coordinates axes |

*Superscript*

| | | |
|---|---|---|
| $'$ | = | fluctuating component |

Presented as Paper 2010-7161 at the 46th AIAA/ASME/SAE/ASEE Joint Propulsion Conference & Exhibit, Nashville, TN, 25–28 July 2010; received 9 January 2010; revision received 12 September 2010; accepted for publication 18 September 2010. 

*Ph.D. Student, School of Aerospace Engineering; zhangqiao_bit@hotmail.com.
†Associate Professor, School of Aerospace Engineering; david78lee@gmail.com (Corresponding Author).
‡Ph.D. Student, School of Aerospace Engineering.
§Professor, School of Aerospace Engineering.

## I. Introduction

SOLID propellant grains are always designed with transition sections in solid rocket motors. While gases with high-temperature flow through the nonuniform port, unstable shear layer could be formed at the sudden transition step and then roll up into vortices, which will impinge on the wall downstream. Acoustic signals will be generated by the impingement and then travel upstream. If the acoustic signals arrive at the vortex source and perturb the shear layer at the right time to contribute to a subsequent vortex, self-sustained periodic oscillation could be formed and instability level would be enhanced in the motor [1].

The analytical model of vortex–acoustic coupling mechanism is based on Powell's theory [2] for subsonic flows in free-field conditions. Howe [3] proposed a generalization to internal flows. To produce sound, the vortices should cross the acoustic streamlines, corresponding to the potential flow streamlines. Vortex–acoustic coupling as a source of oscillation behavior in solid rocket motors has been studied for nearly 40 years. Flandro and Jacobs [4] and Flandro [5] emphasized that the instability of the rocket motor was linked to the hydrodynamic instability of the mean-flow sheared regions. Flandro added rotational flow correction and mean vertical correction flow correction in the linear stability formulations [6,7] and presented a detailed model of the feedback effect that linked the acoustical and vortical fields in the vicinity of the origin of the shear layer. Experiments conducted by Culick and Magiawala [8] and Dunlap and Brown [9] demonstrated coupling of the frequencies of periodic vortex-shedding with those of the acoustic modes in the chamber. They believed that the pressure oscillations occurred when the shedding frequency was close to one acoustic mode frequency. Dotson and Koshigoe [10] studied the thrust characteristics in a Titan IV solid rocket motor upgrade and established the classical four-step model, which contained the loop of vortex generation, vortex impingement, acoustic pulse excitation, and acoustic pulse feedback. After quantities of experiments and analysis on P230, French researchers [11–14] classified vortex-shedding into three categories: obstacle vortex-shedding, corner vortex-shedding, and parietal vortex-shedding. Anthoine et al. [15–17] deduced that the transport velocity vector of vortices was significantly deviated from the acoustical streamlines when they approached the nozzle inlet. The oscillation amplitude increased linearly with the nozzle cavity volume in the submerged nozzle motors and could be reduced by altering the three-dimensional characteristics of vortices.

In recent decades, most of the studies have been related to submerged nozzle configurations in large solid rocket motors.

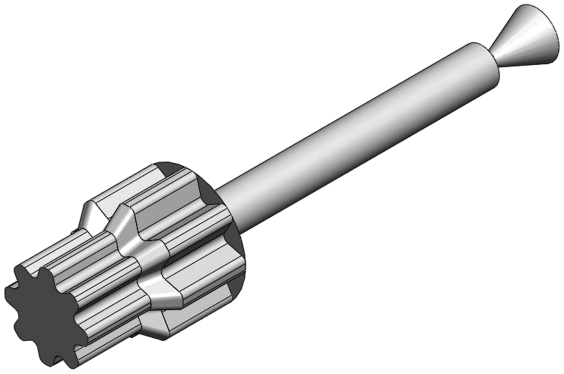

**Fig. 1 Configuration of inner cavity of the tailpipe motor.**

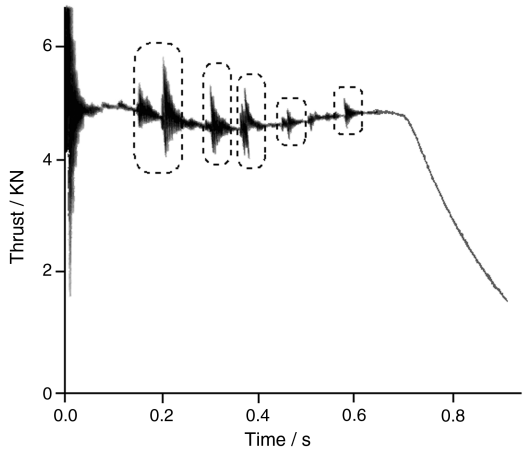


**Fig. 2 Typical thrust history.**

Publications concerning oscillation characteristics in medium- or small-scale motors with tailpipe nozzle are scarcely reported. A single-chamber dual-thrust solid rocket motor with a tailpipe experiences severe thrust oscillations. The propellant is a modified double-base propellant. The inner cavity configuration in Fig. 1 shows that the first-stage grain is composed of two star-shaped grains connected by sudden-change sections. The typical thrust history during the first stage is presented in Fig. 2. Strong thrust oscillations occur for $0.2 < t < 0.6$ s, and the maximum peak-to-peak amplitude reached 40% of the mean thrust. Quite different from any acoustic mode of the chamber (greater than 1000 Hz), the oscillation frequencies extracted from the test are only around 100–200 Hz. Even taking into account the coupling between the motor itself and the testing stand, the amplitudes are still too high. Quantities of methods were proposed to solve this problem, such as digging holes on the grain, changing the number of stars, and even changing the propellant to a nonmetallized type containing stabilizing additives. However, none of these methods show any effect on the low-frequency oscillations characteristics.

In this paper, two commercial codes (FLUENT® and ANSYS®) are used to study the internal flowfield and acoustic field, respectively, in this motor. It is noted that acoustic signals, superimposed on the vortex-shedding motions, will couple with unstable internal flowfield. Three engineering methods, including decreasing transition-section angle of the grain, decreasing convergence angle of the nozzle, and increasing tailpipe radius, are proposed to reduce the potential oscillation amplitude.

## II. Computational Model and Methods

### A. Governing Equations

Both three-dimensional and two-dimensional large-eddy simulation models in FLUENT have been successfully used for predicting oscillation characteristics in solid rocket motors [18–21]. Governing equations are obtained by filtering Navier–Stokes equations on the Fourier space or configuration space. The filter function is defined as [22]

$$G(x, x') = \begin{cases} \frac{1}{V}, & x' \in \upsilon \\ 0, & x' \notin \upsilon \end{cases} \tag{1}$$

where $V$ is the volume of computational cells. The Favre-averaging could eliminate complex triple correlations between density and velocity fluctuations in the governing equations and simplify the governing equations for compressible flows. It is described as

$$\tilde{f} = \frac{\overline{(\rho f)}}{\bar{\rho}} \tag{2}$$

Combustion kinetics and multiphase are neglected in our study. Thus, the filtered form of the governing equations could be written as

$$\frac{\partial \bar{\rho}}{\partial t} + \frac{\partial \bar{\rho} \tilde{u}_i}{\partial x_i} = 0 \tag{3}$$

$$\frac{\partial}{\partial t}(\bar{\rho}\tilde{u}_i) + \frac{\partial}{\partial x_j}(\bar{\rho}\tilde{u}_i\tilde{u}_j) = -\frac{\partial \bar{p}}{\partial x_i} + \frac{\partial}{\partial x_j}(\tilde{\sigma}_{ij} - \tau_{ij}^{\text{sgs}}) \tag{4}$$

$$\frac{\partial}{\partial t}(\bar{\rho}\tilde{e}) + \frac{\partial}{\partial x_i}(\bar{\rho}\tilde{u}_i\tilde{e}) = \frac{\partial}{\partial x_i}(-\bar{p}\tilde{u}_i - \bar{q}_i + \tilde{u}_i\tilde{\sigma}_{ij} - H_i^{\text{sgs}} - \Theta_i^{\text{sgs}}) \tag{5}$$

where the molecular viscosity stress tensor $\tilde{\sigma}_{ij}$ and heat flux $\bar{q}_i$ are given as

$$\tilde{\sigma}_{ij} = \mu\left(\frac{\partial \tilde{u}_i}{\partial x_j} + \frac{\partial \tilde{u}_j}{\partial x_i}\right) - \frac{2}{3}\mu\frac{\partial \tilde{u}_k}{\partial x_k}\delta_{ij} \tag{6}$$

$$\bar{q}_i = -\bar{K}\frac{\partial \tilde{T}}{\partial x_i} \tag{7}$$

The governing equations are supplemented with the equation of state for an ideal gas:

$$p = \rho RT \tag{8}$$

Physical parameters are treated as constants to simplify the calculation, which are listed in Table 1.

The total subgrid stress tensor (sgs) is $\tau_{ij}^{\text{sgs}}$, which can be expressed as

$$\tau_{ij}^{\text{sgs}} = 2\mu_t\left(\tilde{S}_{ij} - \frac{1}{3}\tilde{S}_{kk}\delta_{ij}\right) + \frac{2}{3}\bar{\rho}k^{\text{sgs}}\delta_{ij} \tag{9}$$

where $\tilde{S}_{ij}$ is the Favre-filtered strain rate tensor given by

$$\tilde{S}_{ij} = \frac{1}{2}\left(\frac{\partial \tilde{u}_i}{\partial x_j} + \frac{\partial \tilde{u}_j}{\partial x_i}\right) \tag{10}$$

To complete the closure for the subgrid stresses, the subgrid eddy viscosity $\mu_t$ and the subgrid kinetic energy $k^{\text{sgs}}$ need to be modeled.

The $\mu_t$ is closed by the wall-adapting local eddy-viscosity model [24], which is designed to return the correct wall asymptotic ($y^3$) behavior for wall-bounded flows without requiring a dynamic procedure.

**Table 1 Physical parameters for calculation**

| Physical properties | Value |
|---|---|
| $\mu$ | Sutherland law [23] |
| $C_p$ | 1765 J/kg · K |
| $\gamma$ | 1.22 |
| $Pr$ | 0.75 |
| $M$ | 26 g/mol |

The subgrid kinetic energy $k^{\text{sgs}}$ is given as

$$k^{\text{sgs}} = C_l V^{2/3} \tilde{S}_{ij} \tilde{S}_{ij} \tag{11}$$

where constant $C_l$ is set to 0.0066.

The terms $H_i^{\text{sgs}}$ and $\Theta_i^{\text{sgs}}$ are subgrid enthalpy flux and subgrid viscous work, respectively, which are described as

$$H_i^{\text{sgs}} = \frac{-\mu_t}{Pr} \frac{\partial H_i}{\partial x_i} \tag{12}$$

$$\Theta^{\text{sgs}} = C_\varepsilon \bar{\rho} (k_{\text{sgs}})^{3/2} / V^{1/3} \tag{13}$$

where constant $C_\varepsilon$ is set to 1.1.

To avoid the unphysical oscillations in the solution fields, a bounded central-differencing scheme is selected for continuity, momentum, and energy equations. Second-order implicit formulation is used in an unsteady solver. A Courant–Friedrich–Lewy number of 1 is imposed, and this results in a time step of $1 \times 10^{-6}$ s with the used grid.

### B. Computational Model and Domain

Since the main focus is on the vortex transport characteristics, the grain is simplified into cylinder shape to understand the physical process easily. The computational domain is displayed in Fig. 3, and the geometrical parameters of the motor are shown in Table 2.

Considering that the model is axisymmetric, the domain shown in Fig. 3 is first rotated only 15° with hexahedron cells. Periodic boundary conditions are set on the two sides. Computational grids are stretched toward the wall in both the $x$ and $y$ directions to make sure $y^+ < 2$. The total mesh number is approximated to 1,600,000. Because of the enormous computational cost required, two-dimensional calculations are performed. Although this model does not allow for the three-dimensional vortex-stretching mechanism, it does allow the study to be accurate to some extent to capture the salient features of oscillation characteristics [18,25–27]. All cases discussed in the present study are simulated by two-dimensional large-eddy simulation model. The mesh sensitivity analysis will be presented in Sec. III.

### C. Boundary Conditions

To focus on the formation of a shear layer due to the presence of the sudden-change section, only axis flow is considered at the inlet boundary under the condition of the same mass flux in the motor's head zone. Different cases could be carried out by changing the magnitude of velocity at the inlet and nozzle throat radius. Because the magnitude of velocity is quite different between the boundary layer and centerline, the boundary condition at the inlet could be described as [25]

$$\dot{m} = u_c \sin\left(\frac{\pi}{2} \frac{y}{R_2}\right) \rho \tag{14}$$

where $\rho$ is obtained by user-defined function [22]. Without the consideration of combustion kinetics, the thermodynamic properties are assumed as constants for the present study. The temperature at the inlet section is kept at 3000 K. The supersonic outflow requires no boundary conditions, according to the method of characteristics. The flow variables at the exit are extrapolated from those within the computational domain.

**Table 2 Values of motor parameters**

| Geometrical parameters | Value |
|---|---|
| $R_1$ | 64 mm |
| $R_2$ | 50 mm |
| $R_3$ | Variables |
| $r$ | Variables |
| $L_1$ | 68 mm |
| $L_{\text{loop}}$ | Variables |
| $L_r$ | 5 mm |
| $L$ | Variables |
| $\alpha$ | Variables |
| $\beta$ | 120° |
| $\theta$ | Variables |
| $\eta$ | 23° |

### D. Acoustic Mode Arithmetic

Based on Helmholtz equation in the harmonic acoustic field, the matrix form of acoustic wave function could be described as

$$(\boldsymbol{K}_{\mathbf{f}} - \omega_a^2 \boldsymbol{M}_{\mathbf{f}}) \boldsymbol{p} = 0 \tag{15}$$

where $\boldsymbol{K}_{\mathbf{f}}$ is the acoustic stiffness matrix, $\boldsymbol{M}_{\mathbf{f}}$ is the acoustic mass matrix, $\boldsymbol{p}$ is the eigenvector, and $\omega_a$ is the eigenvalue. After solving this equation by finite element method in ANSYS, the natural acoustic frequency could be calculated as $f_a = \omega_a / 2\pi$.

## III. Results and Discussion

### A. Pressure Oscillation Mechanism

Dotson and Koshigoe [10] deduced the vortex-shedding frequency as follows:

$$f = \frac{U}{L} \left( \frac{m - \alpha}{Ma/(1 - Ma) + 1/k} \right) \tag{16}$$

where $U$ is the freestream velocity, $L$ is the distance between the vortex source and impingement points, $m$ is the number of vortices lying between the vortex source and impingement points, $Ma$ is the Mach number, $\alpha$ is a correction factor that accounts for the delay between the impingement of a vortex and the generation of an acoustic pulse, and $k$ is the ratio of the velocity at which the vortices are convected to the main flow. According to quantities of experiments for large boosters, $\alpha$ is often chosen between 0 and 0.25, and $k$ varies between 0.57 and 0.63.

This mechanism could also be applied to the chamber in the tailpipe motor, which is schematically illustrated in Fig. 4. The zone composed of the dashed line and walls is the vortex–acoustic coupling cavity in the combustion chamber, and its volume is $V_{\text{coupling}}$. Because gases in the converging zone before the tailpipe are typically subsonic, the disturbance due to vortices impingement travels back upstream by speed of sound and perturbs the vortex source to contribute to a subsequent vortex. Similarly, we could estimate that the vortex-shedding frequency increases either with the increase of $U$ or decrease of $L$. However, since $m$, $\alpha$, and $k$ are semi-empirical parameters, computational fluid dynamics is still needed in certain cases.

### B. Instantaneous Flowfield

It is the vorticity magnitude that characterizes vortices intensity. According to the results in this paper, the typical vorticity magnitude

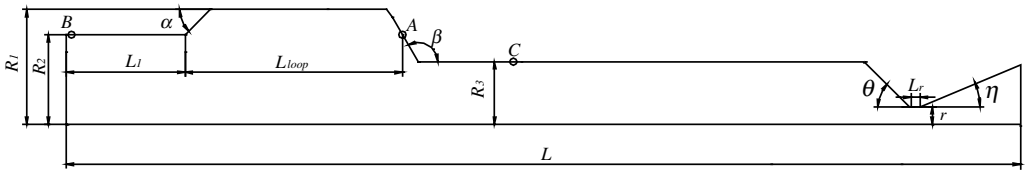


**Fig. 3 Computational model and domain.**

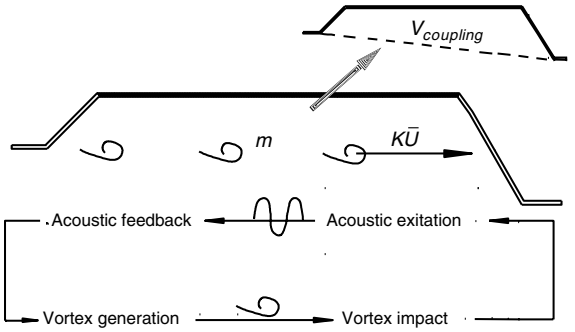


**Fig. 4 Vortex–acoustic coupling model.**

contours in the combustion chamber and tailpipe are shown in Fig. 5. In Fig. 5a, it is apparent that vortices generated at sudden transition step belong to corner vortex-shedding. At the moment of $t$, due to an unsteady shell layer and reverse pressure gradient, strong vortices roll up and then shed downstream. After a period of $\Delta t$, continued vortices shed from the step. Periodic characteristics of internal flowfield are presented in the cavity, as shown in Fig. 5b. After impinging on the converging wall before the tailpipe, the intensity of the former vortex is attenuated. There is a little divergence compared to the large solid rocket motors with submerged nozzle configuration. Since the main flow has been already accelerated close to local sound speed near the submerged nozzle throat, most vortices will be dissipated quickly after impingement in large motors. However, in the tailpipe motor, since the internal flowfield is typically subsonic, the broken vortices will be divided into two parts, as displayed in Fig. 5c. One part of these cracked vortices travels back upstream along with acoustic signals and merges with new vortices shedding from the vortex source, which will impinge on the converging wall again. The others, convected into the tailpipe, will be dissipated quickly for their low intensity.

In the process of shedding, another phenomenon is the pairing of vortices, which was also investigated in Cosyn and Vierendeels's research [27]. It could be conjectured that more than one acoustic mode is superimposed on the vortex-shedding frequency. In Fig. 5c, the parietal vortex-shedding phenomenon could also be observed.

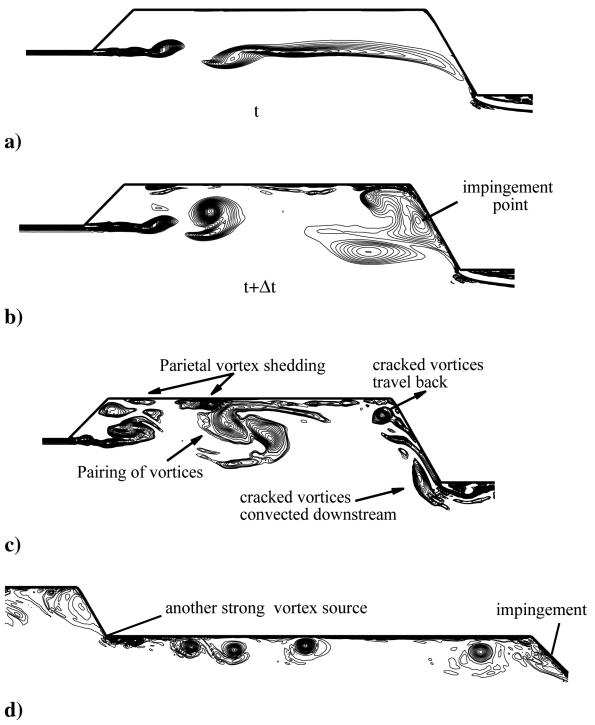


**Fig. 5 Vorticity magnitude contours in the combustion chamber and tailpipe.**

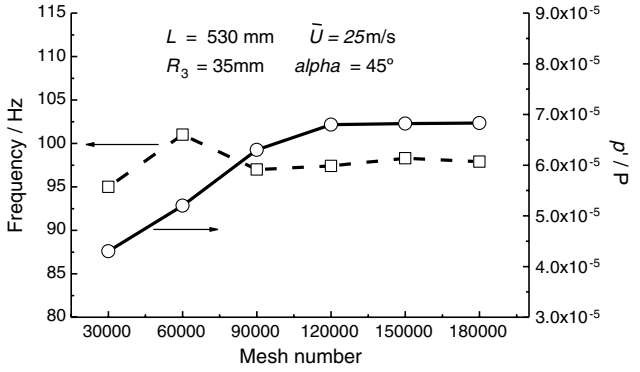


**Fig. 6 Comparison of the most excited frequencies and nondimensional amplitude: mesh sensitivity analysis.**

Vortices shedding from the parietal wall will interact with that from the rearward-facing step to enhance vertical scales in the cavity. Figure 5d shows contours in the tailpipe, and it can be easily noted that another strong vortex source appears at the corner of tailpipe inlet section. Because gases have been accelerated in the first converging zone, vortices shedding from here will be convected downstream with high velocity. Similarly, they will also impinge on the converging wall downstream.

### C. Pressure Oscillation Characteristics

First, the validation of numerical results is conducted by means of a mesh sensitivity analysis. Six different computational meshes are employed for grid validation, ranging from 30,000 (mesh M1) up to 180,000 (mesh M6) mesh points. One specific case with $\bar{U}=$ 25 m/s, $L = 530$ mm, $l_{\text{loop}} = 121$ mm, $R_3 = 35$ mm, $\alpha = 45°$, and $\theta = 45°$ is taken to analyze in detail. The comparison shown in Fig. 6

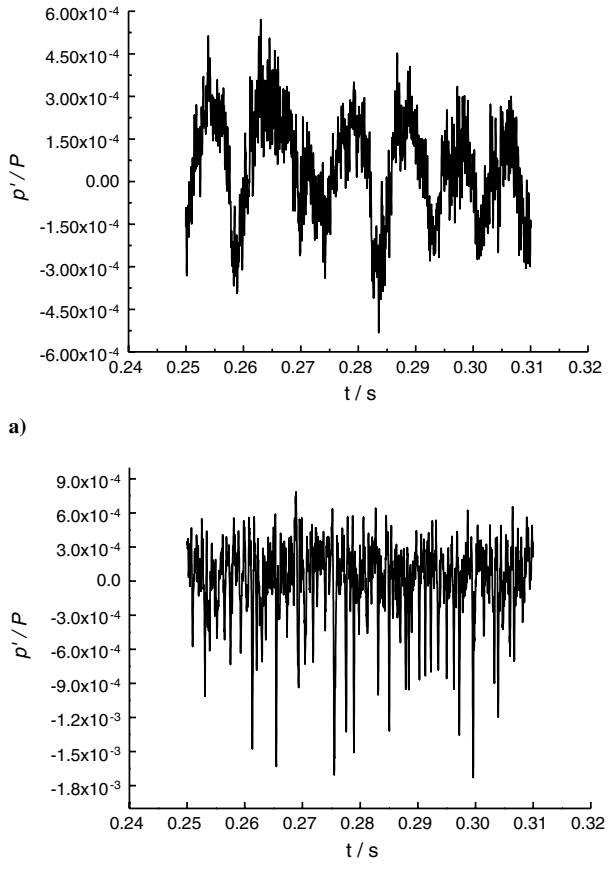


**Fig. 7 Nondimensional pressure oscillation amplitude history of a) virtual sensor A and b) virtual sensor C.**

is carried out considering the most excited frequencies and their amplitude $p'/P$ of virtual sensor A.

From the comparison it is evident that mesh M4 (mesh number 120,000) is sufficiently accurate to reproduce pressure oscillation behavior. From an engineering point of view, it is noteworthy that results from the last three conditions are very similar. Meshes M4 and M5 give a difference of 0.9% in the frequency values and a difference of 0.3% on the nondimensional amplitude. Based on these results, mesh M4 is chosen for the numerical simulations presented in this section.

As displayed in Fig. 3, virtual sensor A is located on the converging wall before the tailpipe. Virtual sensor B is placed on the head end of the motor and virtual sensor C is located at the central section of the tailpipe wall. The pressure oscillation characteristics of these three zones represent the main feature in the motor. Nondimensional pressure oscillation amplitude history of sensors A and C are illustrated in Fig. 7, where $p'$ is oscillation amplitude and $P$ represents the mean pressure of sensors A and C, respectively. Without accounting for combustion kinetics, $p'$ is much smaller than $P$. Each sensor depicts weak oscillations. However, it is obvious that oscillation characteristics in the combustion chamber and tailpipe are different from each other.

Fast Fourier transform (FFT) for virtual sensors A and B is shown in Fig. 8. The spectrum shows that the dominant frequency $f_{\text{low}}$ is 97.4 Hz, which indicates that low-frequency oscillations occur in the combustion chamber. The other two peaks, corresponding to $f_{h1} = 1093$ Hz and $f_{h2} = 2619$ Hz, appear in the high-frequency domain. According to acoustic modal analysis, the fundamental longitudinal oscillation frequency is $f_{1L} = 1103.3$ Hz; the second and the third longitudinal oscillation frequencies are $f_{2L} = 2644$ Hz and $f_{3L} = 3354$ Hz, respectively. It is evident that the low frequency is close to that in the experiment, and other frequencies show great agreement to that extracted from mode analysis. It is so intriguing that pressure oscillations occur when the shedding frequency is so remarkably different from the classical acoustic frequency. This special phenomenon has been investigated by Wu and Kung [28] and Kailasanath et al. [29]. They inferred that there should exist a strong coupling between the quarter-wave acoustic modes and the frequency of large vortical structures. Different from their conclusion, the authors believe that acoustic signals, superimposed on the vortex-shedding frequency, contribute to the periodic oscillation.

Data in the two sensors reflect some different oscillation characteristics. Virtual sensor A is positioned on the converging wall of the tailpipe, which is the sensitive zone of vortex–acoustic coupling. Virtual sensor B is placed on the head end of the motor, which is far from coupling cavity. Thus, the amplitude peak of virtual sensor B on $f_{\text{low}}$ is much smaller than that of virtual sensor A. However, the head end of the motor is an antinode of acoustic pressure and the converging wall of the tailpipe is located close to the pressure node in either fundamental or second longitudinal acoustic mode. Therefore, in the high-frequency domain, the amplitude peaks of virtual sensor A are smaller than those of virtual sensor B.

According to acoustic mode analysis, nondimensional pressure amplitude of the fundamental acoustic mode is depicted in Fig. 9. Because the average diameter of the tailpipe is smaller than that of the combustion chamber, the nondimensional acoustic pressure amplitude in the tailpipe is larger than that in the combustion chamber. FFT for visual sensor C is shown in Fig. 10. Its spectrum reveals the distinct oscillation characteristics in the tailpipe compared with that in the combustion chamber. It is apparent that high frequencies predominate in the pipe, and every peak frequency is so close to a certain longitudinal acoustic frequency. Comparing Fig. 5d, we could investigate that vortices shedding from the vortex source at the tailpipe inlet are convected downstream with high velocity to impinge on the converging wall of the nozzle downstream. This process will also stimulate acoustic pulse. Additionally, experiments from Dunlap and Brown [9] and research by Dotson and Koshigoe [10] indicate that the acoustic mode triggers vortex-shedding more easily at locations where the acoustic pressure features a node. Figure 9 shows that the vortex source at the tailpipe inlet is indeed close to the pressure node. Acoustic pressure amplitude in the tailpipe is larger than that in the combustion chamber. All of these reasons will probably induce high frequencies dominating in the tailpipe.

### D. Variables' Effects on Oscillation Characteristics

In this section, dozens of cases involving different parameters are used to study parameters that influence the oscillation frequency and amplitude in the combustion chamber. In every case, the mean head-end pressure is 11.2 MPa. Considering the high probability of the coupling between vortex, sound, and combustion process, oscillations characteristics in the combustion chamber are the most important in solid rocket motors. Thus, only low-frequency oscillations are taken into account in this paper. All of these analyses are based on data from virtual sensor A.

From Figs. 11 and 12, we find that $f_{\text{low}}$ is mainly influenced by $\bar{U}$ and $L_{\text{loop}}$. Either increasing $\bar{U}$ or decreasing $L_{\text{loop}}$ could reduce the closed-loop time in the vortex–acoustic coupling cycle and increase $f_{\text{low}}$ directly. Generally, this is consistent with Eq. (16). Figure 13 shows the relationship between the excited frequency and the transition-section angle $\alpha$. It is evident that the variation of $f_{\text{low}}$ is less than 17% even if $\alpha$ changes from 20 to 90°, so we can conclude that $\alpha$ has a minor impact on $f_{\text{low}}$.

Combining Figs. 11–13, it is obvious that oscillation amplitude is mainly affected by $\bar{U}$ and $V_{\text{coupling}}$. To consider it from dynamics, increasing $\bar{U}$ will enhance the impulse at the impingement moment; thus, the oscillation amplitude will increase in sequence. Taking one specific case in which $\bar{U} = 100$ m/s and $\alpha = 45°$, for instance, the results show that the maximum zero-peak amplitude is larger than 1 atm. On the other hand, considering the vortex–acoustic coupling

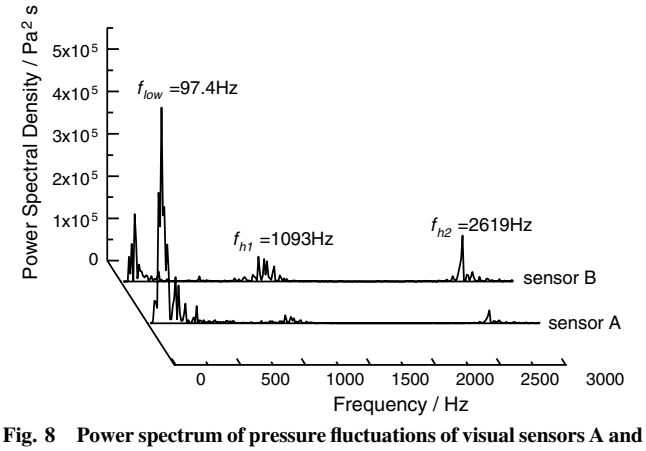


**Fig. 8 Power spectrum of pressure fluctuations of visual sensors A and B.**

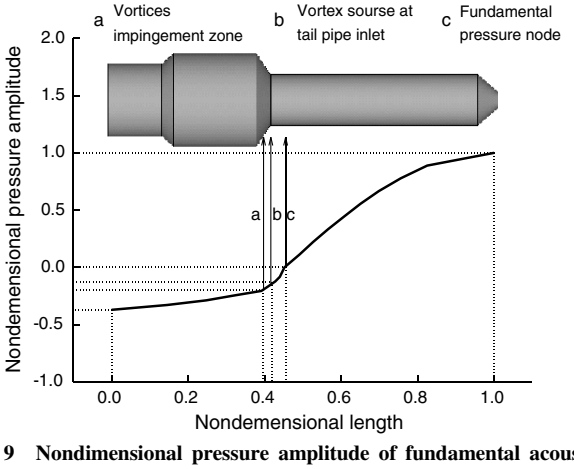


**Fig. 9 Nondimensional pressure amplitude of fundamental acoustic mode.**

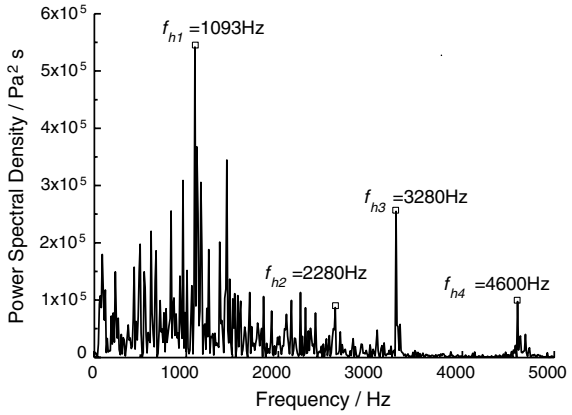


**Fig. 10 Power spectrum of pressure fluctuations of virtual sensor C.**

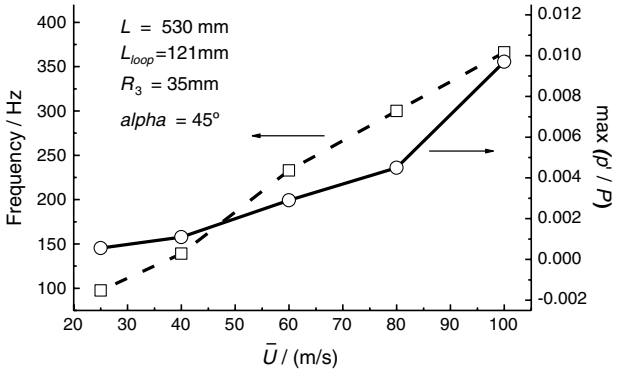


**Fig. 11 Oscillation frequency and maximum nondimensional amplitude variation with $\bar{U}$.**

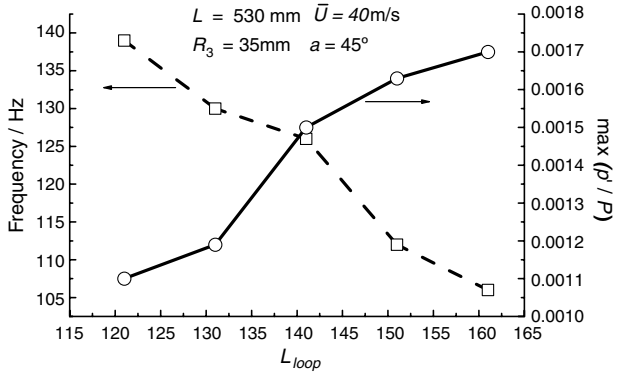


**Fig. 12 Oscillation frequency and maximum nondimensional amplitude variation with $L_{\text{loop}}$.**

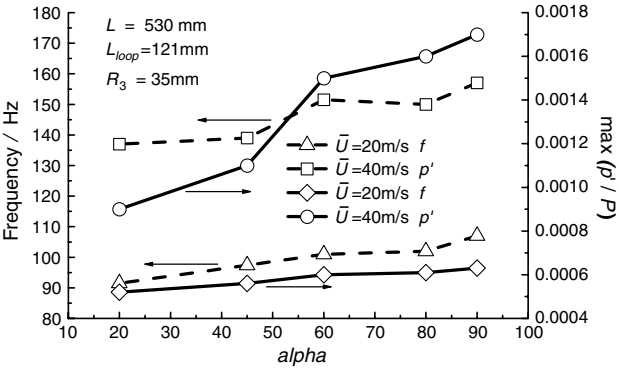


**Fig. 13 Oscillation frequency and maximum nondimensional amplitude variation with $\alpha$.**

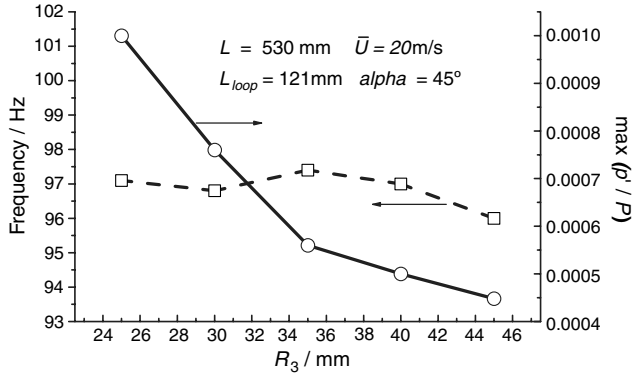


**Fig. 14 Oscillation frequency and maximum nondimensional amplitude variation with $R_3$.**

mechanism, the vortex–acoustic coupling cavity is essentially a resonator. Increasing $L_{\text{loop}}$ and $\alpha$ will directly enlarge the volume of this cavity and then enhance the scale of vortices shedding from the backward step. Meanwhile, more cracked vortices exist in the cavity after impingement. One part of these cracked vortices merges with large vortices shedding from the backward step or parietal wall and then impinging on the converging wall again. The other part, traveling upstream to the backward step, will enhance the probability of the vortex–acoustic coupling. Figure 13 shows that the range of the maximum nondimensional amplitude reaches 88% when $\bar{U}$ is equal to 40 m/s, which is four times larger than that when $\bar{U}$ is 20 m/s. This indicates that $\alpha$ influences oscillation amplitude more remarkably with the increase of $\bar{U}$.

Figure 14 shows the excited frequency and the maximum nondimensional amplitude variation with $R_3$: the radius of the tailpipe. It is found that the change of $f_{\text{low}}$ is limited, but the range of oscillation amplitude is distinct. This could also be explained by $V_{\text{coupling}}$. In all cases, $R_2$ is fixed at 50 mm, so $R_3$ has a close relation with $V_{\text{coupling}}$. If the difference between $R_3$ and $R_2$ is small, the probability that vortices impinge on the converging wall is quite small. Most of these vortices are directly convected into the tailpipe, which leads to small amplitudes. With the increase of the difference between $R_3$ and $R_2$, $V_{\text{coupling}}$ increases sequentially, and the oscillation amplitude increases efficiently. When $R_3$ is reduced to 25 mm, the oscillation amplitude is 2.2 times larger than that when $R_3$ is 45 mm. At the same time, since the difference between $R_3$ and $R_2$ is getting too large, the maximum nondimensional oscillation amplitude of the fundamental longitudinal acoustic mode in the tailpipe is also 1.94 times larger than that when $R_3$ is 45 mm. Neither of these phenomena is beneficial to the motor.

To make an accurate estimation of the oscillation amplitude, it is especially important to account for nozzle losses when the acoustic motions are excited. According to results illustrated in Fig. 15, the convergence angle of the nozzle $\boldsymbol{\theta}$ has a relationship with the nozzle damping to some extent. The combustion chamber is far from the

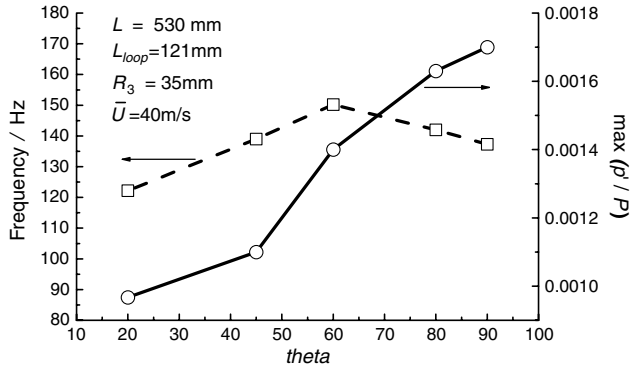


**Fig. 15 Oscillation frequency and maximum nondimensional amplitude variation with $\theta$.**

nozzle; however, from a reasonable design point of view, decreasing $\theta$ could reduce the effective area for acoustic wave reflection and enhance the ability of the nozzle to absorb acoustic energy efficiently. Thus, it is recommended to reduce $\boldsymbol{\theta}$ under the premise of meeting design targets.

By disregarding combustion reactions, nondimensional oscillation amplitudes in all cases are smaller than 1%. However, in practical conditions, pressure oscillations triggered by vortex-shedding are only one aspect in combustion instabilities. The amplitude should be larger than the results in this paper, with the consideration of the comprehensive coupling between vortex, sound, and combustion kinetics.

## IV. Conclusions

A numerical study of the oscillation process in a tailpipe solid rocket motor is conducted by means of a large-eddy simulation technique. The phenomenon in which acoustic signals, superimposed on the vortex-shedding motions, couple with internal flowfield is proven to be one of the main reasons contributing to oscillation in the motor. Low frequencies predominate in the combustion chamber with small acoustic pressure amplitude; otherwise, high frequencies predominate in the tailpipe with large acoustic pressure amplitude. The dominant low frequencies in the combustion chamber are mainly affected by upstream mean velocity and the distance between vortex source and impingement points. Either increasing upstream mean velocity or the volume of vortex–acoustic coupling cavity could enhance the potential oscillation amplitude. Considered from a reasonable design point of view, it is concluded that decreasing sudden transition angle of the grain in conjunction with increasing tailpipe radius could efficiently reduce the potential oscillation amplitude.

## Acknowledgments

The grant support from National Science Foundation of China (no. 51076015) is greatly acknowledged.

## References

[1] Sun, W. S., *Combustion Instabilities in Solid Rocket Motors*, Beijing Institute of Technology Press, Beijing, 1987, Chaps. 1, 5 (in Chinese).

[2] Powell, A., "Theory of Vortex Sound," *Journal of the Acoustical Society of America*, Vol. 36, No. 1, 1964, pp. 177–195. doi:10.1121/1.1918931

[3] Howe, M. S., "Contributions to the Theory of Aerodynamic Sound, with Application to Excess Jet Noise and the Theory of the Flute," *Journal of Fluid Mechanics*, Vol. 71, 1975, pp. 625–673. doi:10.1017/S0022112075002777

[4] Flandro, G. A., and Jacobs, H. R., "Vortex-Generated Sound in Cavities," AIAA Paper 73-1014, Oct, 1973.

[5] Flandro, G. A., "Effects of Vorticity on Rocket Combustion Stability," *Journal of Propulsion and Power*, Vol. 11, No. 4, 1995, pp. 607–625. doi:10.2514/3.23887

[6] Chibli, H. A., Majdalani, J., and Flandro, G. A., "Fundamental Growth Rate Corrections in Rocket Motor Stability Calculations," AIAA Paper 2002-3610, July 2002.

[7] Flandro, G. A., "Aeroacoustic Instability in Rockets," *AIAA Journal*, Vol. 41, No. 3, 2003, pp. 485–497. doi:10.2514/2.1971

[8] Culick, F. E. C., and Magiawala, K., "Excitation of Acoustic Modes in a Chamber by Vortex Shedding," *Journal of Sound and Vibration*, Vol. 64, No. 3, 1979, pp. 455–457. doi:10.1016/0022-460X(79)90591-1

[9] Dunlap, R., and Brown, R. S., "Exploratory Experiments on Acoustic Oscillation Driven by Periodic Vortex Shedding," *AIAA Journal*, Vol. 19, No. 3, 1981, pp. 408–409. doi:10.2514/3.7783

[10] Dotson, K. W., and Koshigoe, S., "Vortex Shedding in a Large Solid Rocket Motor Without Inhibitors at the Segment Interfaces," *Journal of Propulsion and Power*, Vol. 13, No. 2, 1997, pp. 197–206. doi:10.2514/2.5170

[11] Prévost, M., Godon, J. C., and Innegraeve, O., "Thrust Oscillation in Reduced Scale Solid Rocket Motors, Part I: Experimental Investigations," AIAA Paper 2005-4003, July 2005.

[12] Chedevergne, F., and Casalis, G., "Thrust Oscillations in Reduced Scale Motors, Part II: A New Theoretical Approach," AIAA Paper 2005-4000, July 2005.

[13] Chedevergne, F., and Casalis, G., "Detailed Analysis of the Thrust Oscillation in Reduced Scale Solid Rocket motors," AIAA Paper 2006-4424, July 2006.

[14] Chedevergne, F., Casalis, G., and Feraille, T., "Biglobal Linear Stability Analysis of the Flow Induced by Wall Injection," *Physics of Fluids*, Vol. 18, No. 1, 2006, Paper 014103. doi:10.1063/1.2160524

[15] Anthoine, J., Bunchlin, J. M., and Hirschberg, A., "Effect of Nozzle Cavity on Resonance in Large SRM: Theoretical Modeling," *Journal of Propulsion and Power*, Vol. 18, No. 2, 2002, pp. 304–311. doi:10.2514/2.5935

[16] Anthoine, J., Bunchlin, J. M., and Guery, J. F., "Effect of Nozzle Cavity on Resonance in Large SRM: Numerical Simulations," *Journal of Propulsion and Power*, Vol. 19, No. 3, 2003, pp. 374–384. doi:10.2514/2.6141

[17] Anthoine, J., and Mettenleiter, M., "Influence Of Adaptive Control on Vortex-Driven Instabilities in a Scaled Model of Solid Propellant Motors," *Journal of Sound and Vibration*, Vol. 262, No. 5, 2003, pp. 1009–1046. doi:10.1016/S0022-460X(02)01034-9

[18] Mason, D. R., Morstadt, R. A., and Cannon, S. M., "Pressure Oscillation and Structural Vibrations in Space Shuttle RSRM and ETM-3 motors," AIAA Paper 2004-3898, July 2004.

[19] Vetel, J., Plourde, F., and Doan-Kim, S., "Experimental and Numerical Characterizations of Unstable Sources in a Solid Rocket Motor," AIAA Paper 2001-3866, July 2001.

[20] Vetel, J., Plourde, F., Doan-Kim, S., and Guery, J. F., "Numerical Simulations of Wall and Shear Layer Instabilities in Cold Flow Setup," *Journal of Propulsion and Power*, Vol. 19, No. 2, 2003, pp. 297–306. doi:10.2514/2.6111

[21] Plourde, F., Najjar, F. M., Vetel, J., Wasistho, B., Doan-Kim, S., and Balachandar, S., "Numerical Simulations of Wall and Shear-Layer Instabilities in a Cold Flow Set-Up," AIAA Paper 2003-4674, July 2003.

[22] FLUENT Version 6.3.26 User's Guide.

[23] Zhang, Z. S., Cui, G. L., and Xu, C. X., *Theory and Molding of Turbulence*, Tsinghua Univ. Press, Beijing, 1995, Chaps. 7, 8 (in Chinese).

[24] Nicoud, F., and Ducros, F., "Subgrid-Scale Stress Modeling Based on the Square of the Velocity Gradient Tensor," *Flow, Turbulence and Combustion*, Vol. 62, No. 3, 1999, pp. 183–200. doi:10.1023/A:1009995426001

[25] Apte, S. V., and Yang, V., "Unsteady Flow Evolution in Porous Chamber with Surface Mass Injection, Part 1: Free Oscillation," *AIAA Journal*, Vol. 39, No. 8, 2001, pp. 1577–1586. doi:10.2514/2.1483

[26] Apte, S. V., and Yang, V., "Unsteady Flow Evolution in a Porous Chamber with Surface Mass Injection, Part 2: Acoustic Excitation," *AIAA Journal*, Vol. 40, No. 2, 2002, pp. 244–253. doi:10.2514/2.1666

[27] Cosyn, P., and Vierendeels, J., "Numerical Simulation of Aeroacoustic Phenomena in a Solid Rocket Booster," *Journal of Spacecraft and Rockets*, Vol. 42, No. 1, 2005, pp. 111–117. doi:10.2514/1.3579

[28] Wu, W. J., and Kung, L. C., "Determination of Triggering Condition of Vortex-Driven Acoustic Combustion Instability in Rocket Motors," *Journal of Propulsion and Power*, Vol. 16, No. 6, 2000, pp. 1022–1029. doi:10.2514/2.5672

[29] Kailasanath, K., Gardner, J. H., Boris, J. P., and Oran, E. S., "Interactions Between Acoustic and Vortex Structures in a Central Dump Combustor," AIAA Paper 1986-1609, July 1986.

T. Lin
*Associate Editor*